

Statistical imprints of CMB B -type polarization leakage in an incomplete sky survey analysis

Larissa Santos,^{*} Kai Wang, Yangrui Hu, Wenjuan Fang, and Wen Zhao[†]

CAS Key Laboratory for Researches in Galaxies and Cosmology,
Department of Astronomy, University of Science and Technology of China,
Chinese Academy of Sciences, Hefei, Anhui 230026, China

(Dated: December 13, 2016)

One of the main goals of modern cosmology is to search for primordial gravitational waves by looking on their imprints in the B -type polarization in the cosmic microwave background radiation. However, this signal is contaminated by various sources, including cosmic weak lensing, foreground radiations, instrumental noises, as well as the E -to- B leakage caused by the partial sky surveys, which should be well understood to avoid the misinterpretation of the observed data. In this paper, we adopt the E/B decomposition method suggested by Smith in 2006, and study the imprints of E -to- B leakage residuals in the constructed B -type polarization maps, $\mathcal{B}(\hat{n})$, by employing various statistical tools. We find that the effects of E -to- B leakage are negligible for the B -mode power spectrum, as well as the skewness and kurtosis analyses of \mathcal{B} -maps. However, if employing the morphological statistical tools, including Minkowski functionals and/or Betti numbers, we find the effect of leakage can be detected at very high confidence level, which shows that in the morphological analysis, the leakage can play a significant role as a contaminant for measuring the primordial B -mode signal and must be taken into account for a correct explanation of the data.

PACS numbers: 95.85.Sz, 98.70.Vc, 98.80.Cq

I. INTRODUCTION

The temperature and polarization anisotropies of the cosmic microwave background (CMB) radiation are powerful cosmological observables to understand the physics of the early universe. During the past decades, much effort has been made to characterize the CMB, including three satellite generations: the cosmic background explorer (COBE), the Wilkinson microwave anisotropy probe (WMAP) and Planck. These experiments were mainly devoted to measure the CMB temperature anisotropies, precisely mapping these tiny fluctuations in the sky [1, 2]. However, according to the standard cosmological model, the full information of CMB is encoded in the statistical properties of both temperature, $T(\hat{\gamma})$, and the linear polarizations, described by the stocks parameters, $Q(\hat{\gamma})$ and $U(\hat{\gamma})$, which are defined with respect to a fixed coordinate system in the sky, and depend on the choice of coordinate system. It is then convenient to decompose the linear polarization into the curl-free (E -mode) and divergence-free (B -mode) components since they have the advantage of being rotationally invariant [3, 4].

Recent results from the Planck satellite also show precise measurements of the E -mode field [5]. In the standard cosmological model, both CMB temperature and E -mode anisotropies are mainly generated by the primordial density perturbations. In addition, the auto-correlation power spectra C_ℓ^{TT} and C_ℓ^{EE} and the cross-correlation power spectrum C_ℓ^{TE} sensitively depend on the cosmological parameters and cosmological models. Thus, the observations of WMAP and Planck satellites on these spectra have tightly constrained most cosmological parameters and inflationary parameters. However, the B -mode polarization encodes quite different cosmological information: In the large scales, the B -mode polarization is supported to be generated by the primordial gravitational waves [3, 4, 6], which is the smoking-gun evidence of inflation [7]. In the small scales, the B -mode is mainly produced by the deflection of the CMB photons by cluster of galaxies during their travel between the last scattering surface and the observer, known as the CMB lensing [8–10]. During the past few years, many ground-based experiments were designed to measure the B -mode polarization signal, such as SPTPol [11], POLARBEAR [12], ACTPol [13], BICEP2 and Keck Array [14–17]. These experiments, including the Planck satellite [18], have detected the lensed B -mode signal in the high multipole range at the high confidence level. Thus, the detection of the primordial B -mode signal is then the main goal of future CMB experiments [19]. Among them we can cite BICEP3, AdvACT, CLASS, Simons Array, SPT-3G, C-BASS, QUIJOTE, EBEX, QUBIC, QUIET, PIPER, Spider, LSPE, et al. [20] as ground-based experiments, and LiteBIRD [21], CMBPOL [22], CoRE [23], PRISM [24], PIXIE [25] as the next satellite generation of CMB experiments.

In the real observations, the detection of cosmological B -mode is limited by various contaminations, including instrumental noises, instrumental systematical errors [26], as well as the polarized foregrounds [27, 28]. Another source of contamination is the so-called E - B mixture, which arises from an incomplete sky analysis of the CMB polarization signals [29]. Our ability

^{*}larissa@ustc.edu.cn

[†]wzhao7@ustc.edu.cn

to decompose CMB polarization signal in a partial sky coverage is crucial, since even for satellite missions the presence of non-cosmological contaminations must be masked out. So, this mixture exists in all the CMB polarization analysis, and could become the dominant contamination for the detection of primordial gravitational waves [29]. In order to solve this problem, numerous practical methods have been developed to separate the E -mode and B -mode in the partial sky [30–34]. However, most of these methods suffer from one or several of the following drawbacks - they are slow in practice, they are difficult to realize in pixel space, and/or they lead to partial information loss. For instance, the method suggested by Bunn et al. (this method is adopted by BICEP2/Keck Array collaboration [14, 17]) involves constructing an eigenbasis, and it has a high computational cost [30, 35]. Among all these methods, the methods proposed in [32–34] are based on a common algebraic framework of the so-called χ -fields. Therefore, they are fast and can be efficiently applied to high resolution maps due to the use of a fast spherical harmonics transformation. However, it is important to mention that the residual of the E -to- B leakage is unavoidable even if the proper method is applied in the data analysis [36]. In the previous work [37], the authors carefully compared these three methods, and they found that although all of them allow a significant reduction of the level of the E -to- B leakage, the method of Smith [32] ensures the smallest error bars in all experimental configurations and leads to the smallest leakage residuals. For these reasons, in the present article, we shall focus on this method due to our limited computational resources, and study the influence of residuals of E -to- B leakage on the CMB B -mode polarization.

In most previous works [32, 37], the authors focused only on the power spectrum of the B -type polarization and that the E -to- B leakage is tiny in the Smith's E/B decomposition method. However, the B -mode is a highly non-gaussian field due to the different kind of components in the observed maps. Thus, in addition to the power spectrum, various non-gaussian statistical tools are also helpful to separate the different components and/or constrain the cosmological parameters. In the previous work [38], we have applied the Minkowski functionals (MFs) to quantify the deviation from Gaussianity of B -mode maps, and studied the effects of instrumental noises, the CMB mask, and the influence of foreground residuals. As an extension of this work, in the present paper, by applying a similar analysis we will focus on characterizing the imprint of the E - B mixture residual in the lensed B -mode map. As well known, MFs characterize the morphological properties of convex, compact sets in an n -dimensional space [39–45]. Moreover, the E -to- B leakage has completely different morphological properties from the stochastic B -mode generated by cosmological sources. We expect the influence of the E -to- B leakage to be significant in the MFs analysis, even if the amplitude of this leakage is small. As the a complementary analysis, in this paper we shall also apply other statistical tools, including the Betti numbers, skewness and kurtosis, to investigate the imprints of E -to- B leakage. Throughout this paper, in order to focus on the effect of E -to- B leakage residuals, we shall consider the case with only cosmic variance and ignore the effects of the other B -mode sources, including the instrumental noises and foregrounds, which have been detail studied in the previous work [38].

The paper is divided as follows: In Sec. II we briefly introduce the theory of CMB polarization. In Sec. III, we derive the equations needed to obtain the E/B decomposition in a partial sky analysis. Sec. IV is divided in 3 subsections: Sec. IV A is devoted to the introduction of the MF statistics, Sec. IV B details the methodology used in this paper, and Sec. IV C describes the results obtained for the MFs. In Sec. V, we use other statistics in the analysis for completeness, being the Betti numbers described in Sec. V A, and both skewness and kurtosis explained in Sec. V B. Finally, in Sec. VI, we draw our conclusions.

II. E - AND B -MODE POLARIZATION OF CMB

The linearly polarized CMB polarization field is completely described by two Stokes parameters, Q and U that can be combined into a spin-(-2) and spin-(+2) fields $P_{\pm}(\hat{n}) = Q(\hat{n}) \pm iU(\hat{n})$. For full sky, the spin fields can be expanded over spin-weighted harmonic functions basis as follows [46]:

$$P_{\pm}(\hat{n}) = \sum_{\ell m} a_{\pm 2, \ell m} \pm 2 Y_{\ell m}(\hat{n}). \quad (1)$$

Alternatively, the polarization field can be written as the curl-free E , and divergence-free B components, which are defined in terms of the coefficients $a_{\pm 2, \ell m}$ in the harmonic space as

$$E_{\ell m} \equiv -\frac{1}{2}[a_{2, \ell m} + a_{-2, \ell m}], \quad B_{\ell m} \equiv -\frac{1}{2i}[a_{2, \ell m} - a_{-2, \ell m}]. \quad (2)$$

In the same way as the temperature field, we can define the $E(\hat{n})$ and $B(\hat{n})$ polarization sky maps in terms of spherical harmonics,

$$E(\hat{n}) \equiv \sum_{\ell m} E_{\ell m} Y_{\ell m}(\hat{n}), \quad B(\hat{n}) \equiv \sum_{\ell m} B_{\ell m} Y_{\ell m}(\hat{n}). \quad (3)$$

The power spectra can then be written as

$$C_\ell^{EE} \equiv \frac{1}{2\ell+1} \sum_m \langle E_{\ell m} E_{\ell m}^* \rangle, \quad (4)$$

$$C_\ell^{BB} \equiv \frac{1}{2\ell+1} \sum_m \langle B_{\ell m} B_{\ell m}^* \rangle, \quad (5)$$

where the brackets denote the average over all realizations. For a Gaussian field, all the statistical properties can be obtained by analyzing the second-order power spectra. It is important to emphasize, however, that here we are dealing with a highly non-Gaussian lensed B -map due to the contribution of CMB lensing to the final map [38]. In this case, different statistics, as, for example, the MFs, are necessary to describe the field. Moreover, we notice that the E/B decomposition in a full sky analysis is straightforward, providing a direct link to the primordial cosmological perturbations, especially the GWs imprint on the CMB B -mode polarization. Nevertheless, we know that Galactic foregrounds are present even in full sky surveys, and they should be masked to reduce the contaminations. So, in the realistic case, we must derive the E -type and B -type maps from the incomplete Q and U observables.

III. E - AND B -MODE DECOMPOSITION IN PARTIAL SKY

If the polarization fields are not measured in full sky, but on a fraction only, Eqs.(2) cannot be derived directly. So, the separation of pure E - and B -mode from the observed Q and U maps is not trivial, due to the existence of ambiguous mode [30], which can be successfully avoided by different ways [30–34]. As mentioned above, in this paper, we adopt the method suggested in [32], which is based on the algebraic framework of the so-called χ -field (denoted as \mathcal{B} -field in the present paper).

For the full-sky observations, according to [47], we can define a new set of fields \mathcal{E} and \mathcal{B} from the polarization fields Q and U as follows:

$$\mathcal{E}(\hat{n}) = -\frac{1}{2} [\bar{\partial} \bar{\partial} P_+(\hat{n}) + \partial \partial P_-(\hat{n})], \quad (6)$$

$$\mathcal{B}(\hat{n}) = -\frac{1}{2i} [\bar{\partial} \bar{\partial} P_+(\hat{n}) - \partial \partial P_-(\hat{n})], \quad (7)$$

where $\bar{\partial}(\partial)$ corresponds to the spin-raising (lowering) operator for an arbitrary function f with spin s ,

$$\bar{\partial} f \equiv -\sin^s \theta \left(\frac{\partial}{\partial \theta} + \frac{i}{\sin \theta} \frac{\partial}{\partial \phi} \right) (f \sin^{-s} \theta), \quad (8)$$

$$\partial f \equiv -\sin^{-s} \theta \left(\frac{\partial}{\partial \theta} - \frac{i}{\sin \theta} \frac{\partial}{\partial \phi} \right) (f \sin^s \theta). \quad (9)$$

From the definition, we know that the new map \mathcal{E} in Eq. (6) is the standard scalar field, and \mathcal{B} in (7) is the pseudo-scalar field in the two-dimensional sphere. Thus, they can be expanded in the spherical harmonics as follows,

$$\mathcal{E}(\hat{n}) \equiv \sum_{\ell m} \mathcal{E}_{\ell m} Y_{\ell m}(\hat{n}), \quad \mathcal{B}(\hat{n}) \equiv \sum_{\ell m} \mathcal{B}_{\ell m} Y_{\ell m}(\hat{n}), \quad (10)$$

where the expanding coefficients are

$$\mathcal{E}_{\ell m} = \int \mathcal{E}(\hat{n}) Y_{\ell m}^*(\hat{n}) d\hat{n}, \quad \mathcal{B}_{\ell m} = \int \mathcal{B}(\hat{n}) Y_{\ell m}^*(\hat{n}) d\hat{n}. \quad (11)$$

These coefficients are related to the regular multipoles $E_{\ell m}$ and $B_{\ell m}$ by

$$\mathcal{E}_{\ell m} = N_{\ell,2} E_{\ell m}, \quad \mathcal{B}_{\ell m} = N_{\ell,2} B_{\ell m}, \quad (12)$$

where we have $N_{\ell,s} = \sqrt{(\ell+s)!/(\ell-s)!}$ [47]. The corresponding power spectra are then obtained as

$$C_\ell^{\mathcal{E}\mathcal{E}} \equiv \frac{1}{2\ell+1} \sum_m \langle \mathcal{E}_{\ell m} \mathcal{E}_{\ell m}^* \rangle = N_{\ell,2}^2 C_\ell^{EE}, \quad (13)$$

$$C_\ell^{\mathcal{B}\mathcal{B}} \equiv \frac{1}{2\ell+1} \sum_m \langle \mathcal{B}_{\ell m} \mathcal{B}_{\ell m}^* \rangle = N_{\ell,2}^2 C_\ell^{BB}. \quad (14)$$

Considering the mask window function $W(\hat{n})$, the masked B -type polarization map becomes $\mathcal{B}W(\hat{n})$, and the pseudo multipole coefficients can be defined as follows [48],

$$\tilde{\mathcal{B}}_{\ell m} = \int d\hat{n} W(\hat{n}) \mathcal{B}(\hat{n}) Y_{\ell m}^*(\hat{n}). \quad (15)$$

So, the pure B -type map $\mathcal{B}W(\hat{n})$ and the coefficient set $\tilde{\mathcal{B}}_{\ell m}$ are mathematically equivalent by definition. In the previous work [33], we have developed a method to directly construct the pure map $\mathcal{B}W(\hat{n})$ from the masked observables Q and U . While in the method [32], we should first construct the pure coefficients $\tilde{\mathcal{B}}_{\ell m}$ and then translate them into the map $\mathcal{B}W(\hat{n})$. However, it is important to emphasize that in both methods, it is impossible to construct the pure B -maps directly. In this paper, we shall adopt the latter method, which is briefly reviewed as follows.

In this method, the concept of pure pseudo-multipoles is put forward and defined as,

$$\mathcal{B}_{\ell m}^{\text{pure}} \equiv -\frac{1}{2i} \int d\hat{n} \left\{ P_+(\hat{n}) [\bar{\partial}\bar{\partial} (W(\hat{n}) Y_{\ell m}(\hat{n}))]^* - P_-(\hat{n}) [\bar{\partial}\bar{\partial} (W(\hat{n}) Y_{\ell m}(\hat{n}))]^* \right\}. \quad (16)$$

It can be proved that this definition is equivalent to the Eq. (15) [32], which shows that in principle the pure pseudo-multipole method can successfully extract the pure B -type polarization signal and avoid the E - B mixing part. To calculate the expression of Eq. (16), we use the property of spin raising and lowering operators and obtain that [37]

$$\begin{aligned} \mathcal{B}_{\ell m}^{\text{pure}} = & -\frac{1}{2i} \int d\hat{n} \left[P_+ \left((\bar{\partial}\bar{\partial} W) Y_{\ell m}^* + 2N_{\ell,1} (\bar{\partial} W) ({}_1Y_{\ell m}^*) + N_{\ell,2} W ({}_2Y_{\ell m}^*) \right) \right. \\ & \left. - P_- \left((\bar{\partial}\bar{\partial} W) Y_{\ell m}^* - 2N_{\ell,1} (\bar{\partial} W) (-{}_1Y_{\ell m}^*) + N_{\ell,2} W (-{}_2Y_{\ell m}^*) \right) \right]. \end{aligned} \quad (17)$$

This expression is used in the following calculations.

Note that, in this method, the first and second derivatives of the window function W are used. If we adopt the top-hat window function, these derivatives diverge in the numerical computations. So, in practice, we should properly smooth the window function to avoid the divergence at the observed patch boundaries. Thus, an appropriate sky apodization will play an important role in suppressing the E -to- B leakage. In the previous work [36], we carefully compare the leakage residual and the information loss for different smoothing methods, and found that the Gaussian smoothing method presented by [49] induces the smallest leakage in the final B -map¹. The Gaussian smoothing kernel used to smooth the edges of W is defined as [49],

$$W_i = \begin{cases} \int_{-\infty}^{\delta_i - \frac{\delta_c}{2}} \frac{1}{\sqrt{2\pi}\sigma^2} \exp\left(-\frac{x^2}{2\sigma^2}\right) dx = \frac{1}{2} + \frac{1}{2} \text{erf}\left(\frac{\delta_i - \frac{\delta_c}{2}}{\sqrt{2}\sigma}\right) & \delta_i < \delta_c \\ 1 & \delta_i > \delta_c \end{cases} \quad (18)$$

where $\sigma = \theta_F / \sqrt{8 \ln 2}$ and θ_F denotes the full width at half maximum of the smoothing kernel. δ_i the smallest angular distance between the i -th observed pixel and the boundary of the mask. δ_c is an adjustable parameter referred as the apodization length. Let β denotes the jump range at $\delta_i = \delta_c$ and $\delta_i = 0$, which is (for details see [49]):

$$\beta = \frac{1}{2} - \frac{1}{2} \text{erf}\left(\frac{\frac{\delta_c}{2}}{\sqrt{2}\sigma}\right). \quad (19)$$

β is a small and adjustable parameter, which must be chosen by investigating the reconstruction numerical accuracy of a smoothed mask performed using the HEALPix package [36]. Here we should mention that performing a spherical harmonic transformation of the foreground mask and its later reconstruction by inverse transformation leads to an oscillation pattern around jump discontinuities (i.e. the reconstructed mask has non-zero values where they were originally zero), called the Gibbs phenomenon. The discrepancy between the original mask and the reconstructed one must be corrected by choosing a window function in which multipoles higher than the truncation point are suppressed.

¹ In the previous works [32], the authors discovered the optimal smoothing function to minimize the errors of the constructed power spectra C_{ℓ}^{BB} , which is dependent of the multipole ℓ . However, different from them, in this paper we shall only focus on the statistical properties of the constructed \mathcal{B} -map. So, we choose the window function for different aim, which should minimize the E - B leakage and reduce the information loss.

IV. THE IMPRINT OF E -TO- B LEAKAGE AND MINKOWSKI FUNCTIONALS ANALYSIS

A. Minkowski Functionals

The MFs describe the morphological properties of convex, compact sets in an n -dimensional space. They provide a powerful statistical tool that can also be used in partial sky maps, detecting non-gaussianities without previous knowledge of their intensity or angular dependence [39–45]. On a two-dimensional CMB field defined on the sphere, \mathcal{S}^2 , the morphological properties of the data can be characterized as a linear combination of three MFs: the area, contour length and integrated geodetic curvature of an excursion set (the latter also known as the difference between the numbers of hot and cold spots)[40, 44]. For a pixelized CMB sphere, an excursion set is given by the number of pixels in which the temperature exceeds the threshold ν . For a given threshold ν , it is convenient to define the excursion set Q_ν and its boundary ∂Q_ν of a smooth scalar field u as follows,

$$Q_\nu = \{x \in \mathcal{S}^2 | u(x) > \nu\sigma\}, \quad (20)$$

$$\partial Q_\nu = \{x \in \mathcal{S}^2 | u(x) = \nu\sigma\}. \quad (21)$$

Thus, the area $v_0(\nu)$, the contour length $v_1(\nu)$ and the integrated geodetic curvature $v_2(\nu)$, can be written as [44]:

$$v_0(\nu) = \int_{Q_\nu} \frac{da}{4\pi}, \quad v_1 = \int_{\partial Q_\nu} \frac{dl}{16\pi}, \quad v_2 = \int_{\partial Q_\nu} \frac{\kappa dl}{8\pi^2}, \quad (22)$$

where da and dl are the surface element of \mathcal{S}^2 and the line element along ∂Q_ν , respectively. The geodetic curvature is represented by k . The MFs can be numerically calculated for a given pixelized map $u(x_i)$ as follows [44, 50]:

$$v_0(\nu) = \frac{1}{N_{\text{pix}}} \sum_{k=1}^{N_{\text{pix}}} \Theta(u - \nu), \quad (23)$$

$$v_i(\nu) = \frac{1}{N_{\text{pix}}} \sum_{k=1}^{N_{\text{pix}}} \mathcal{I}_i(\nu, x_k), \quad (i = 1, 2). \quad (24)$$

In Eq. (23), the Heaviside step function is represented by Θ . In Eq. (24), we define \mathcal{I} such that

$$\mathcal{I}_1(\nu, x_k) = \frac{\delta(u - \nu)}{4} \sqrt{u_{;\theta}^2 + u_{;\phi}^2}, \quad \mathcal{I}_2(\nu, x_k) = \frac{\delta(u - \nu)}{2\pi} \frac{2u_{;\theta}u_{;\phi}u_{;\theta\phi} - u_{;\theta}^2u_{;\phi\phi} - u_{;\phi}^2u_{;\theta\theta}}{u_{;\theta}^2 + u_{;\phi}^2}. \quad (25)$$

Expressing the covariant derivatives at a point $x = (\theta, \phi)$, parameterized through the azimuth angle θ and the polar angle ϕ of the unite sphere, we have [44]:

$$u_{;\theta} = u_{,\theta}, \quad u_{;\phi} = \frac{1}{\sin\theta}u_{,\phi}, \quad u_{;\theta\theta} = u_{,\theta\theta}, \quad (26)$$

$$u_{;\theta\phi} = \frac{1}{\sin\theta}u_{,\theta\phi} - \frac{\cos\theta}{\sin^2\theta}u_{,\phi}, \quad u_{;\phi\phi} = \frac{1}{\sin^2\theta}u_{,\phi\phi} + \frac{\cos\theta}{\sin\theta}u_{,\theta}. \quad (27)$$

In this paper, we shall investigate the statistical properties of the E -to- B leakage and its possible imprint in the CMB B -mode polarization field due to a partial sky analysis. We used the algorithm developed by [51] and [52] for calculating the MFs.

B. Method

First, we generate two groups of Monte Carlo simulations containing 500 full-sky Q and U lensed maps each. The first group of simulation corresponds to a tensor-to-scalar ratio $r = 0$, and the second corresponds to $r = 0.1$. We used the LensPix software [58] with cosmological parameters $h^2\Omega_b = 0.0223$, $h^2\Omega_c = 0.1188$, $h = 0.673$, $A_s = 2.1 \times 10^{-9}$, $n_s = 0.9667$, $\tau_{\text{reio}} = 0.066$ and $N_{\text{side}} = 1024$. As mentioned above, in the numerical calculations, the numerical errors caused by the high multipoles are quite significant for two reasons: First, the errors caused by the Gibbs phenomenon is dominant by the high multipoles [49]; Second, the \mathcal{BB} power spectrum is quite tilde blue, and the high multipoles dominate the numerical errors in the HEALPix-based computations [33]. Similar to the previous works [33, 36], in order to smooth the high multipoles, we apply a Gaussian smoothing with the parameter full width half maximum FWHM = $30'$. We also smooth the edges of the Planck

polarization mask UT78pol, using Eqs. (18) and (19) with $\delta_c = 1^\circ$ and $\beta = 10^{-4}$ [36] to obtain our window function, shown in Fig. 1. With this in mind, we point out the steps of our analysis, which are divided in two parts. In the first case (named as *real case* in this paper), in order to mimic the realistic data analysis, we simulate the full-sky Q and U maps, and mask by adopting the proper mask. Then, applying the E/B decomposition method in [32, 37] we obtain the partial ‘pure’ B -type polarization map $\mathcal{B}(\hat{n})$. In the second case (named as *ideal case* in this paper), we derive the coefficients $B_{\ell m}$ from the full-sky Q and U maps, and translate them to the corresponding $\mathcal{B}_{\ell m}$. Thus, we can construct the full-sky \mathcal{B} -maps by the standard route. Then, we mask them by applying exactly same mask in the first case. Comparing the \mathcal{B} -maps in these two cases, we find that the maps derived in the real case include the residual E -to- B leakage caused by the E/B decomposition method. However, the maps derived from the ideal case are free from it [33]. So, the difference between these two kinds of \mathcal{B} -maps reflect the imprints of residual E -to- B leakage, which is the main goal of this article. To realize it, we do our analysis by the following steps:

- *Real case*: First, we obtain the E/B decomposition from partial Q and U lensed sky maps as numerically described in [37]. For each of the derived BW -map, we can define the pseudo power spectrum as $\tilde{C}_\ell^{\mathcal{B}\mathcal{B}} = \frac{1}{2\ell+1} \sum_m \tilde{\mathcal{B}}_{\ell m} \tilde{\mathcal{B}}_{\ell m}^*$, where $\tilde{\mathcal{B}}_{\ell m} = \int BW(\hat{n}) Y_{\ell m}^*(\hat{n}) d\hat{n}$. In Fig. 2, we plot the average power spectra $\tilde{C}_\ell^{\mathcal{B}\mathcal{B}}$ for the model with $r = 0$ and $r = 0.1$ with solid black and blue lines, respectively. As mentioned above, these power spectra include two parts: One is the CMB B -type polarization, the other is the residual E -to- B leakage. In order to show the contribution of the residual leakage, we do the exact same analysis to the model with $r = 0$ and no CMB lensing (i.e. no CMB B -mode). Thus, the derived BW -maps only include the residual E -to- B leakage. From Fig. 1, we find that the residuals are quite significant around the two poles and two belts at $\theta = 48^\circ$ and $\theta = 132^\circ$, which are caused by the structure of the HEALPix package. The corresponding power spectrum is also present in Fig. 2 (blue line), which is much smaller than the spectra including CMB signals, in particular in the low-multipole range. However, in the high-multipole range, the residuals become more and more important, and dominate the power spectrum at $\ell \gtrsim 1200$, which is consistent with the previous works [32, 33, 36].
- Second, it is well known that the calculation of the MFs requires smoothing the maps to be analyzed in order to remove the contribution of multipoles dominated by noise. Even though different smoothing scales of the same CMB map have a high correlation, they must be taken into account in order to extract all its available statistical information. This is based on the fact that for each smoothing scale, the information of the CMB is dominant in a different multipole range [51, 54, 56]. Thus, we smooth each final \mathcal{B} -map with $N_{\text{side}} = 1024$ and FWHM = $30'$ using a Gaussian filter with a smoothing scale, θ_s , such that $W_l = \exp\left[\frac{1}{2}\ell(\ell+1)\theta_s^2\right]$ with $\theta_s = 10', 20', 30', 40', 50', 60'$, generating 6 sets of 500 maps.
- Third, we apply three different sky cuts to the final \mathcal{B} -maps: the smoothed (for each θ_s) apodized window function derived from the Planck UT78 polarization mask (hereafter, sky cut 1), to exclude the pixels already without any CMB information; the Planck mask + two bands centered at 48° and 132° , both with width of 6° to avoid the E -to- B stripe residuals (hereafter, sky cut 2), and Planck mask + the two residual bands + a 20° width cut around the poles, also to avoid the E -to- B residuals in these regions (hereafter, sky cut 3), see the upper panel right side of Fig. 1. For each smoothing scale, we excluded every pixel of the window function with values less than 0.9 in order to remove the boundary effects. We statistically analyze the final 6 sets of 500 \mathcal{B} -map simulations for each sky cut by means of the MFs for both groups with $r = 0$ and $r = 0.1$. Note that the binning range of the threshold ν is set from -3 to 3 with 25 equally spaced bins.
- *Ideal case*: First, we obtain the E/B decomposition in full-sky Q and U lensed sky maps directly using the HEALPix subroutine anafast. The $B_{\ell m}$ coefficients must be then multiplied by $N_{\ell,2}$ (see Eqs. (11) and (12)) before generating the full-sky \mathcal{B} -maps using the synfast subroutine of HEALPix. Then, we mask these \mathcal{B} -maps by applying the smoothed Planck UT78pol mask. Similar to the real case, we also calculate the corresponding power spectra $\tilde{C}_\ell^{\mathcal{B}\mathcal{B}}$, which are presented in Fig. 2 in dashed lines. Comparing with the results in the real case, we find that the spectra are same in both cases, which validates the effectiveness of the E/B decomposition method.
- The second and third steps are exactly the same as for the real case.
- We finally compare the MFs of both cases, the one that the E -to- B leakage is present (real) and the one that it is not (ideal), in order to identify the possible signature of the leakage in the MFs. We quantify the difference between the ideal and real cases by means of the χ^2 statistics, defined as

$$\chi^2 = \sum_{aa'} [\bar{v}_a^{\text{ideal}} - \langle v_a^{\text{real}} \rangle] C_{aa'}^{-1} [\bar{v}_{a'}^{\text{ideal}} - \langle v_{a'}^{\text{real}} \rangle], \quad (28)$$

where $\langle v_a^{\text{real}} \rangle$ is the model under test. For each smoothing factor, θ_s , a and a' denote the binning number of the threshold value ν and the different kinds of MF. For the total χ_T^2 , a and a' also denote θ_s . The covariance matrix is estimated from the average under 500 simulations $C_{aa'} \equiv \frac{1}{499} \sum_{k=1}^{500} \left[(v_a^{k,\text{real}} - \bar{v}_a^{\text{real}}) (v_{a'}^{k,\text{real}} - \bar{v}_{a'}^{\text{real}}) \right]$.

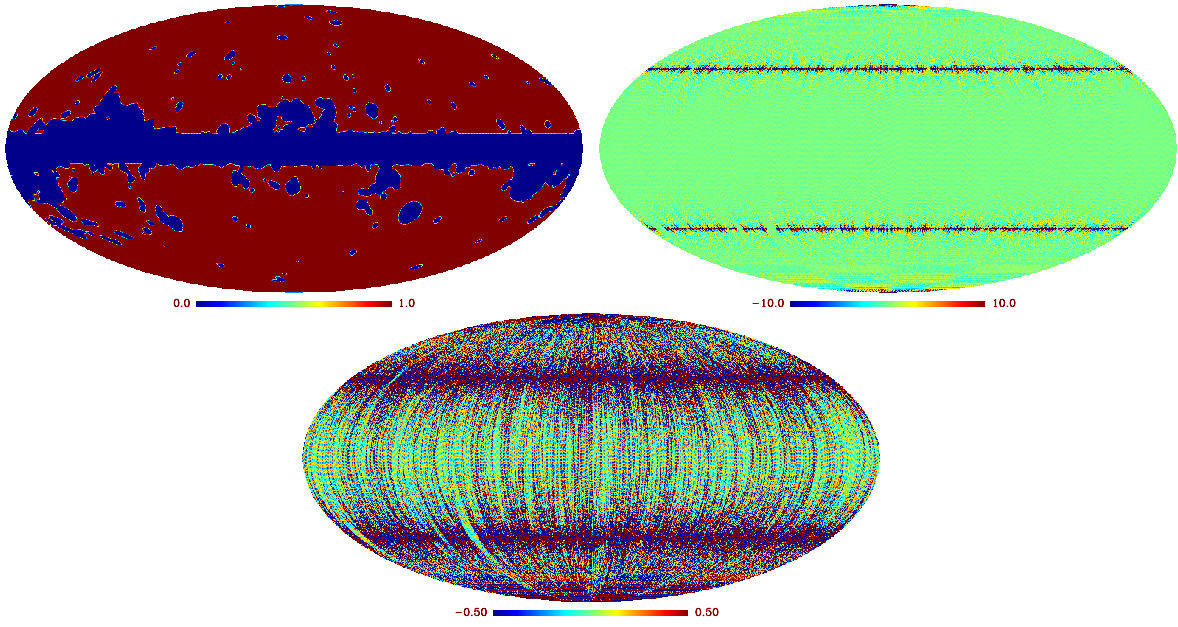


FIG. 1: Upper panel: On the left, the Gaussian smoothed window function considering Planck UT78 polarization mask with parameters $\beta = 10^{-4}$ and $\delta_c = 1^\circ$. On the right, the residuals of E -to- B leakage in μK for $r = 0$ when CMB lensing is not taken into account. Lower panel: the same map shown in the right side of the upper panel rescaled.

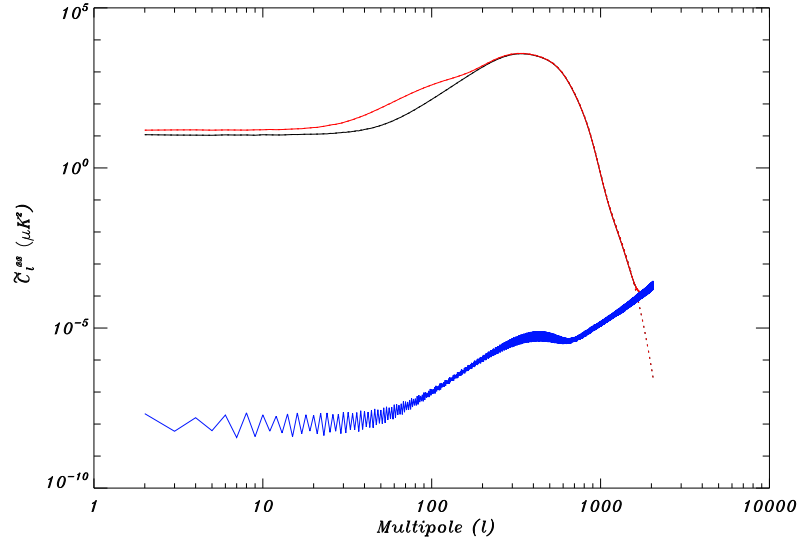


FIG. 2: The mean power spectra of 500 simulations considering $r = 0$ (black lines) and $r = 0.1$ (red lines) for the ideal (dashed lines) and real (solid lines) cases. The blue solid curve is the mean power spectrum of 500 simulations considering $r = 0$ and no CMB lensing for the real case (power spectrum related to the E -to- B leakage).

C. Results

In real CMB observations, the Galactic emission must be masked out even considering data obtained from satellite surveys. The CMB polarization, especially the B -mode signal, is the main target of future experiments since it can probe inflation. However, this primordial signal can be hidden behind the foregrounds: instrumental noise, different astrophysical foregrounds and CMB lensing (see [38] for a detailed study of the statistics of these different secondary B -mode signals). Moreover, dealing with partial sky maps, leads to a leakage between E and B modes that could also mimic the primordial signal.

First, let's consider the case in which there is no primordial gravitational waves, $r = 0$. After proceeding with the E/B

decomposition, we applied to our simulations the sky cuts described in Sec. IV B for each smoothing parameter, θ_s : The UT78pol Planck mask alone, UT78pol + contamination bands, and UT78pol + contamination bands + poles. Our aim is to avoid both Galactic foreground and the E -to- B leakage (check Fig. 1). Calculating the MFs for the final \mathcal{B} -map simulations and using Eq. (31) to obtain the χ^2 statistics, we get the results shown in Table I. They quantify the significance of the leakage for each smoothing scale and sky cut. We find that, by increasing θ_s the significance of the leakage becomes much smaller, which significantly shows that the leakage is dominated by the high multipoles, which is consistent with the results of power spectrum shown in Fig. 2. We can see this result more clear in Fig. 4, where we plotted v_0, v_1, v_2 (in Eq. (22)) for $\theta_s = 10', 40', 60'$ in the case $r = 0$. Even though the significance of the leakage seen in Table I also decreases when we exclude the pixels where the leakage is more evident, the contamination bands and the poles, its imprint is still noticeable in the MFs analysis. We conclude that the contamination bands and the poles do not play a very important role in the overall leakage contribution, as we can also see in the lower panel of Fig. 1, where we rescaled the unlensed \mathcal{B} -map with $r = 0$ to point out the leakage contribution.

	$\theta_s = 10'$	$\theta_s = 20'$	$\theta_s = 30'$	$\theta_s = 40'$	$\theta_s = 50'$	$\theta_s = 60'$
Sky cut 1	18.93	9.53	4.27	1.62	0.71	0.34
Sky cut 2	17.27	8.55	3.80	1.42	0.63	0.30
Sky cut 3	15.78	7.97	3.56	1.28	0.57	0.27

TABLE I: χ^2 for $r = 0$ and three different sky cuts: the UT78pol Planck mask alone, UT78pol + contamination bands, and UT78pol + contamination bands + poles.

Now, considering both cases, without ($r = 0$) and with primordial gravitational waves ($r = 0.1$), and applying the UT78 Planck polarization mask only, we find no significant change in the χ^2 between them, as shown in Table II. For the larger tensor-to-scalar ratio, the effect of leakage is slightly amplified for smaller θ_s . We can compare the results for the three MFs in Fig. 4 with $\theta_s = 10', 40', 60'$ ($r = 0$) with the same results for $r = 0.1$ in Fig. 5.

	$\theta_s = 10'$	$\theta_s = 20'$	$\theta_s = 30'$	$\theta_s = 40'$	$\theta_s = 50'$	$\theta_s = 60'$
$\chi^2 (r = 0)$	18.93	9.53	4.27	1.62	0.70	0.34
$\chi^2 (r = 0.1)$	21.18	11.00	4.41	1.63	0.62	0.29

TABLE II: The χ^2 for different smoothing parameters and different models for the difference between ideal and real case, considering only the UT78pol mask.

This latter result is more obvious when we analyze the total χ^2 combining all smoothing parameters in Eq. (31). We can see in Table III that the effect of the E -to- B leakage is more evident for $r = 0.1$. Comparing Tables II and III, we can also notice by the large values of the total χ^2 for both models that the MFs for different smoothing scales are very correlated. It is easy to understand this since the E -to- B leakage is not a stochastic noise, and it is always relevant in the same sky regions. The total χ^2 is then obtained considering the correlation coefficients $\rho_{aa'} = C_{aa'}/\sqrt{C_{aa}C_{a'a'}}$ instead of a direct sum of the χ^2 values for each smoothing scale, θ_s . Note that, in Fig. 3, we did not use the last binning value of the threshold ν since it approaches zero for the first MF for every θ_s in order to avoid numerical problems. It is then important to point out that even though the leakage seems not relevant for individual smoothing scales, it is definitely relevant when they are combined as shown in Table III. The E -to- B leakage should be carefully considered when analyzing partial sky CMB B -mode data in order to avoid misinterpretation of the data.

	$r = 0$	$r = 0.1$
χ_T^2	220.23	268.74

TABLE III: The total χ^2 of MFs analysis for different models, considering only the UT78pol mask.

V. OTHER STATISTICS

In order to further investigate the imprint of residual E -to- B leakage in the constructed \mathcal{B} -maps, in this section, we shall consider the other statistical tools (Betti numbers, skewness, kurtosis), which are the complementary of analysis based on MFs and power spectrum.

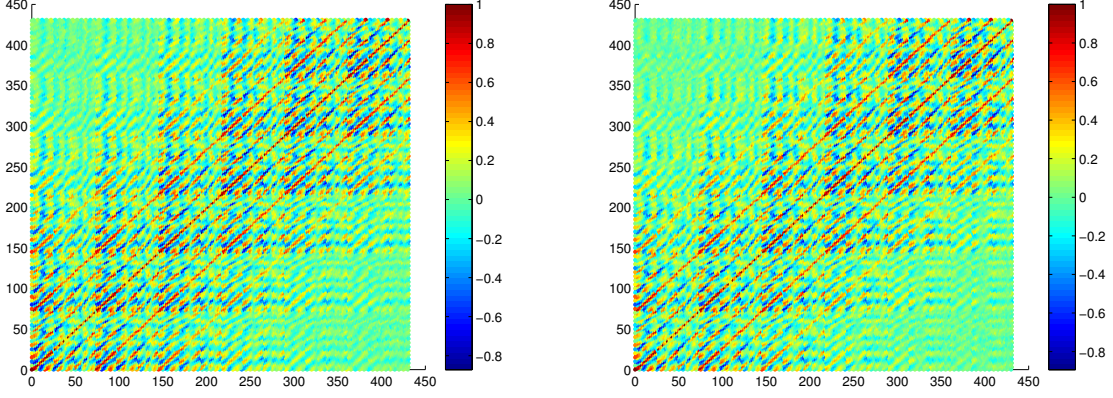


FIG. 3: The correlation coefficient values, $\rho_{aa'} = C_{aa'}/\sqrt{C_{aa}C_{a'a'}}$, for $r = 0$ (left panel), and for $r = 0.1$ (right panel) are represented by the colors. The axis correspond to a and a' : the binning number of the threshold value, the different kinds of MFs and the smoothing scale. Both panels correspond to the calculations when only the UT78 Planck polarization mask is considered (sky cut 1).

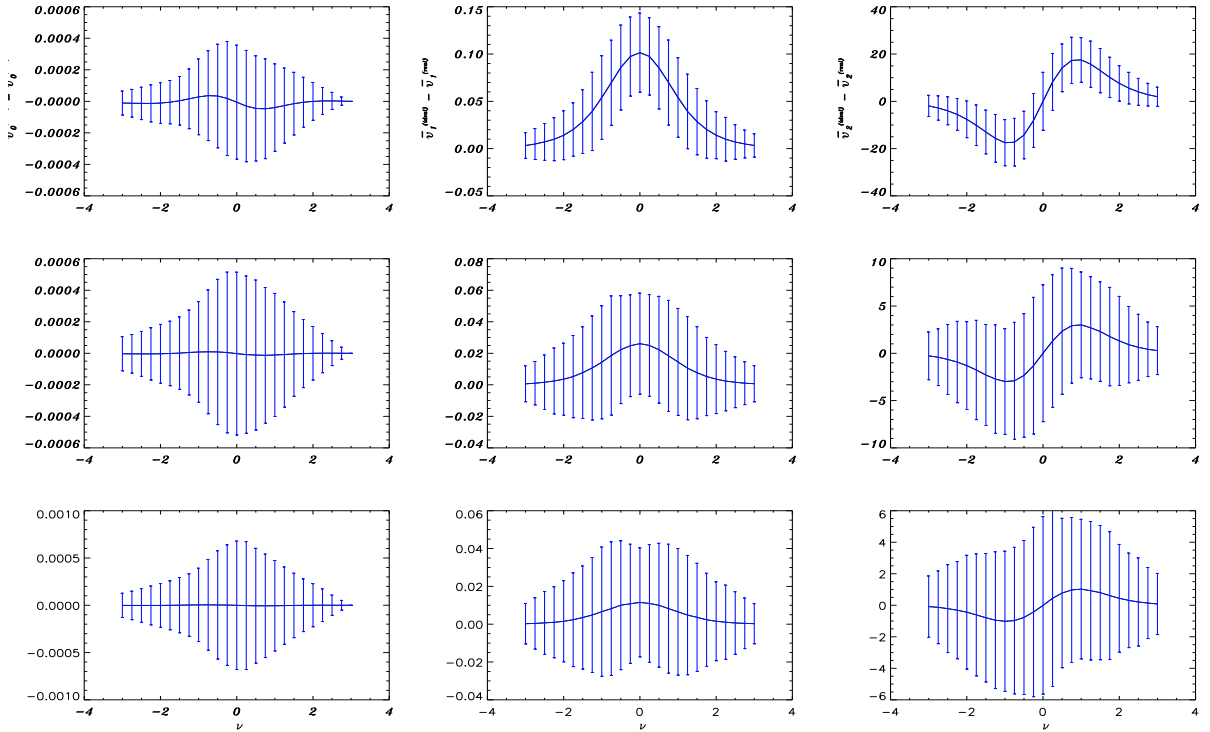


FIG. 4: The difference between the mean values of real and ideal case for the MFs considering $r = 0$ over 500 simulations. From top to bottom: $\theta_s = 10', 40', 60'$, respectively. From left to right: the first, second and third MF, respectively.

A. Betti numbers

The morphological properties of the excursion sets can be also quantified in terms of topological quantities called the Betti numbers. They provide an intuitive understanding of the topology of isosurfaces. For a two-dimensional manifold, such as the CMB field, there are two non-zero Betti numbers. The excursion set consists of many connected regions (number of hot spots) β_0 , and independent tunnels (number of cold spots) β_1 . For each threshold ν , we can mathematically express β_0 and β_1 as line

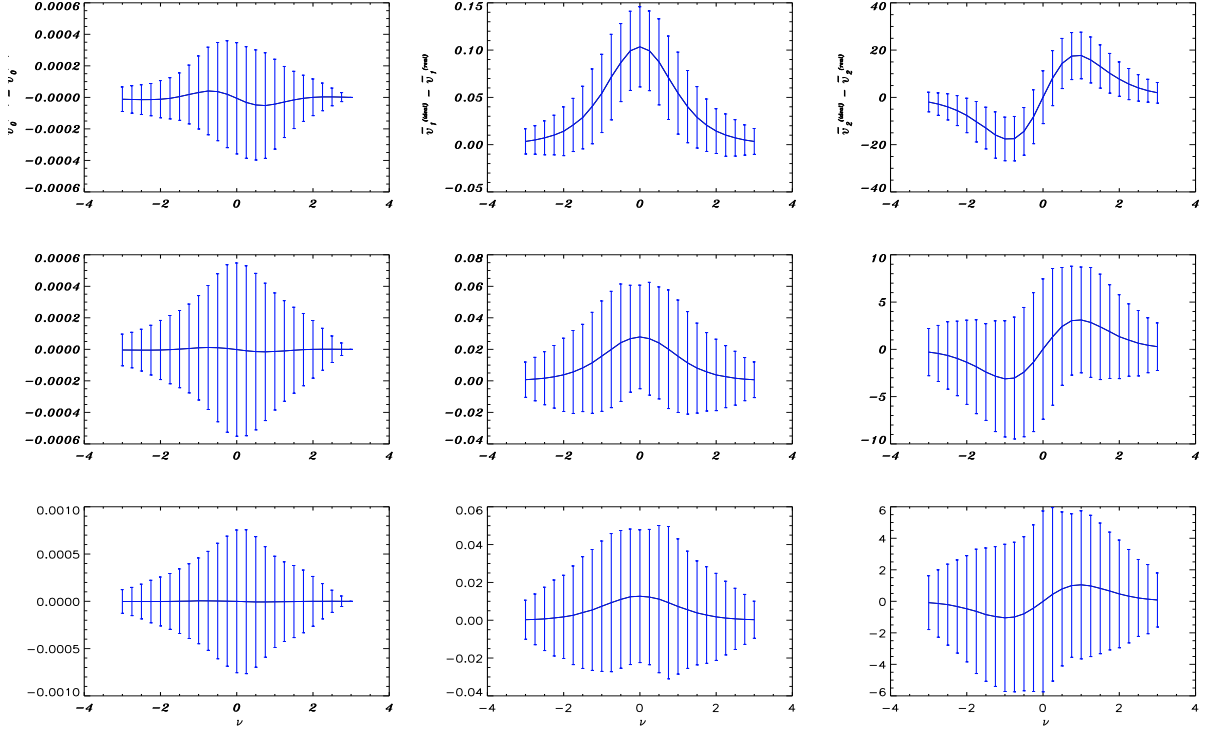


FIG. 5: The difference between the mean values of real and ideal case for the MFs considering $r = 0.1$ over 500 simulations. From top to bottom: $\theta_s = 10', 40', 60'$, respectively. From left to right: the first, second and third MF, respectively.

integrals [53, 55]:

$$\beta_0 = \frac{1}{2\pi} \int_{C_+} k dl, \quad \beta_1 = \frac{1}{2\pi} \int_{C_-} k dl, \quad (29)$$

where C_+ and C_- denote the contours that enclose hot and cold spots, respectively. k is the total curvature of iso-temperature contours for each threshold ν . Thus, the genus, g , is given by a linear combination of β_0 and β_1 as $g(\nu) = \beta_0(\nu) - \beta_1(\nu)$. The numerical method for computing the Betti numbers is outlined in [53, 55].

Following the same steps outlined in Sec. IV B and using the exact same 500 \mathcal{B} -mode simulated maps, we calculated β_0 and β_1 for both real and ideal cases considering both $r = 0$ and $r = 0.1$. The imprint of the leakage in the Betti number results were obtained by considering

$$\Delta\beta_i = \beta_i^{ideal} - \beta_i^{real}, \quad (30)$$

where $i = 0, 1$ represent the Betti numbers or alternatively, the number of hot and cold spots.

To quantify the difference between the ideal and real cases, we again use the χ^2 statistics

$$\chi^2 = \sum_{aa'} [\bar{\beta}_a^{ideal} - \langle \beta_a^{real} \rangle] C_{aa'}^{-1} [\bar{\beta}_{a'}^{ideal} - \langle \beta_{a'}^{real} \rangle]. \quad (31)$$

For each smoothing factor θ_s , a and a' denote the binning number of the threshold value ν and the two Betti numbers. We notice by Fig. 7 (for $r = 0$) and 8 (for $r = 0.1$) that our results are qualitatively consistent with the ones obtained for the MFs: The significance of the leakage becomes smaller as θ_s increases. Moreover, we found that the quantitative results of the χ^2 statistics considering each individual smoothing scale for the Betti numbers are also in agreement with the results found for the MFs (compare Tables IV and V with I and Tables II), supporting the method and providing a consistency check for our calculations. Finally, as for the total χ^2 , we see from Table VI that the imprint of the E -to- B leakage becomes less evident when compared with the results for the MFs (Table III). It is important to emphasize, however, that there is more information encoded in the MFs analysis, especially considering all the correlation coefficients when the smoothing scales are combined (compare Figs. 3 and 6). The calculation of the Betti numbers is strongly related to the third MF v_2 [53, 55].

	$\theta_s = 10'$	$\theta_s = 20'$	$\theta_s = 30'$	$\theta_s = 40'$	$\theta_s = 50'$	$\theta_s = 60'$
Sky cut 1	24.14	11.47	4.64	1.84	0.74	0.35
Sky cut 2	22.31	10.45	4.17	1.53	0.64	0.30
Sky cut 3	19.17	9.11	3.93	1.46	0.60	0.28

TABLE IV: χ^2 for $r = 0$ and three different sky cuts, considering the Betti numbers: the UT78pol Planck mask alone, UT78pol + contamination bands, and UT78pol + contamination bands + poles.

	$\theta_s = 10'$	$\theta_s = 20'$	$\theta_s = 30'$	$\theta_s = 40'$	$\theta_s = 50'$	$\theta_s = 60'$
$\chi^2 (r = 0)$	24.14	11.47	4.64	1.84	0.74	0.35
$\chi^2 (r = 0.1)$	23.70	12.31	5.12	1.97	0.75	0.34

TABLE V: The χ^2 for different smoothing parameters and different models for the difference between ideal and real case Betti numbers, considering only the UT78pol mask.

	$r = 0$	$r = 0.1$
χ_T^2	79.70	75.74

TABLE VI: The total χ^2 of Betti numbers analysis for different models, considering only the UT78pol mask.

B. Skewness and kurtosis

In this subsection, for the cross-check, we apply the one-point statistics, skewness and kurtosis to search for the imprints of E -to- B leakage. We calculated the skewness, the lack of symmetry in a distribution, and the kurtosis, the degree to which the distribution is peaked, for the 500 B -mode simulations considering both ideal and real cases and the 6 smoothing parameters mentioned previously ($\theta_s = 10', 20', 30', 40', 50', 60'$).

The results in Tables VII and VIII show the mean values and standard deviation for both statistics considering $r = 0$ and $r = 0.1$, which show that no evidence of the leakage was found neither in the skewness nor in the kurtosis statistics (we see no deviations in the results comparing the ideal and real cases). These analyzes indicate that, different from the MFs and Betti numbers, the skewness and kurtosis statistics are not sensitive enough to probe the imprints of residual E -to- B leakage in the constructed B -maps. The skewness histograms of these simulations for the ideal and real cases considering both $r = 0$ and $r = 0.1$ are shown in Figs. 9 and 10, respectively. The histograms were also plotted for the kurtosis statistics, as can be seen in Figs. 11 and 12, for $r = 0$ and $r = 0.1$, respectively. These figures are consistent with the results listed in Tables VII and VIII, i.e. the differences between ideal case and real case are not significant.

	$\theta_s = 10'$	$\theta_s = 20'$	$\theta_s = 30'$	$\theta_s = 40'$	$\theta_s = 50'$	$\theta_s = 60'$
$r = 0$	-0.00057 ± 0.00530	-0.00059 ± 0.00560	-0.00040 ± 0.00606	0.00002 ± 0.00669	0.00040 ± 0.00735	0.00058 ± 0.00802
$r = 0.1$	-0.00057 ± 0.00530	-0.00059 ± 0.00561	-0.00039 ± 0.00607	0.00002 ± 0.00670	0.00040 ± 0.00735	0.00058 ± 0.00802
	0.00005 ± 0.00525	0.00008 ± 0.00567	0.00013 ± 0.00630	0.00017 ± 0.00705	0.00018 ± 0.00779	0.00021 ± 0.00872
	0.00005 ± 0.00526	0.00008 ± 0.00568	0.00013 ± 0.00630	0.00017 ± 0.00705	0.00018 ± 0.00779	0.00021 ± 0.00872

TABLE VII: The skewness values (mean value and the standard deviation) for the simulated B -mode polarization maps. For each case, the upper one shows the results derived from the ideal case, while the lower one shows those derived for the real case. In both cases we use 500 lensed B -maps simulations and the UT78pol mask only.

	$\theta_s = 10'$	$\theta_s = 20'$	$\theta_s = 30'$	$\theta_s = 40'$	$\theta_s = 50'$	$\theta_s = 60'$
$r = 0$	0.627 ± 0.018	0.530 ± 0.018	0.427 ± 0.019	0.338 ± 0.019	0.266 ± 0.019	0.207 ± 0.008
	0.625 ± 0.018	0.529 ± 0.018	0.426 ± 0.019	0.338 ± 0.019	0.266 ± 0.019	0.207 ± 0.008
$r = 0.1$	0.587 ± 0.017	0.482 ± 0.017	0.367 ± 0.017	0.264 ± 0.017	0.179 ± 0.017	0.113 ± 0.018
	0.584 ± 0.017	0.480 ± 0.017	0.365 ± 0.017	0.263 ± 0.017	0.178 ± 0.017	0.113 ± 0.018

TABLE VIII: The kurtosis values (mean value and the standard deviation) for the simulated B -mode polarization maps. For each case, the upper one shows the results derived from the ideal case, while the lower one shows those derived for the real case. In both cases we use 500 lensed B -maps simulations and the UT78pol mask only.

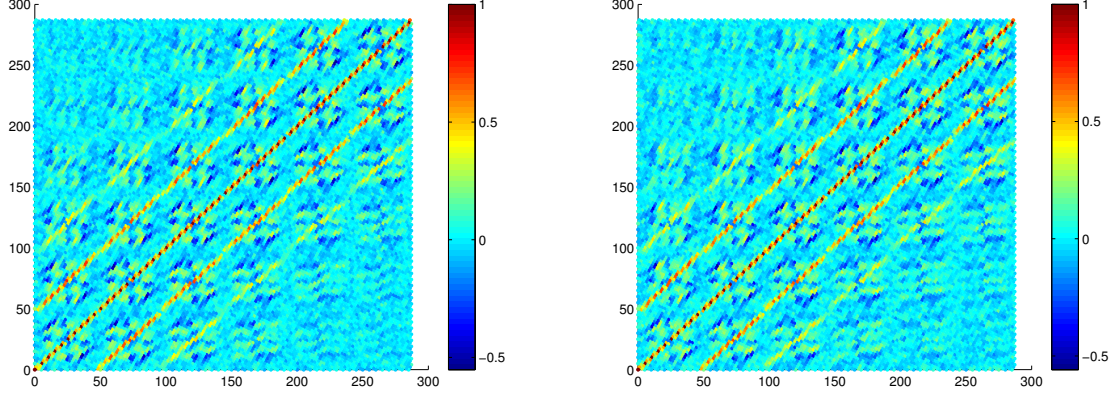


FIG. 6: The correlation coefficient values, $\rho_{aa'} = C_{aa'}/\sqrt{C_{aa}C_{a'a'}}$, for $r = 0$ (left panel), and for $r = 0.1$ (right panel) are represented by the colors. The axis correspond to a and a' : the binning number of the threshold value, the two Betti numbers and the smoothing scale. Both panels correspond to the calculations when only the UT78 Planck polarization mask is considered (sky cut 1).

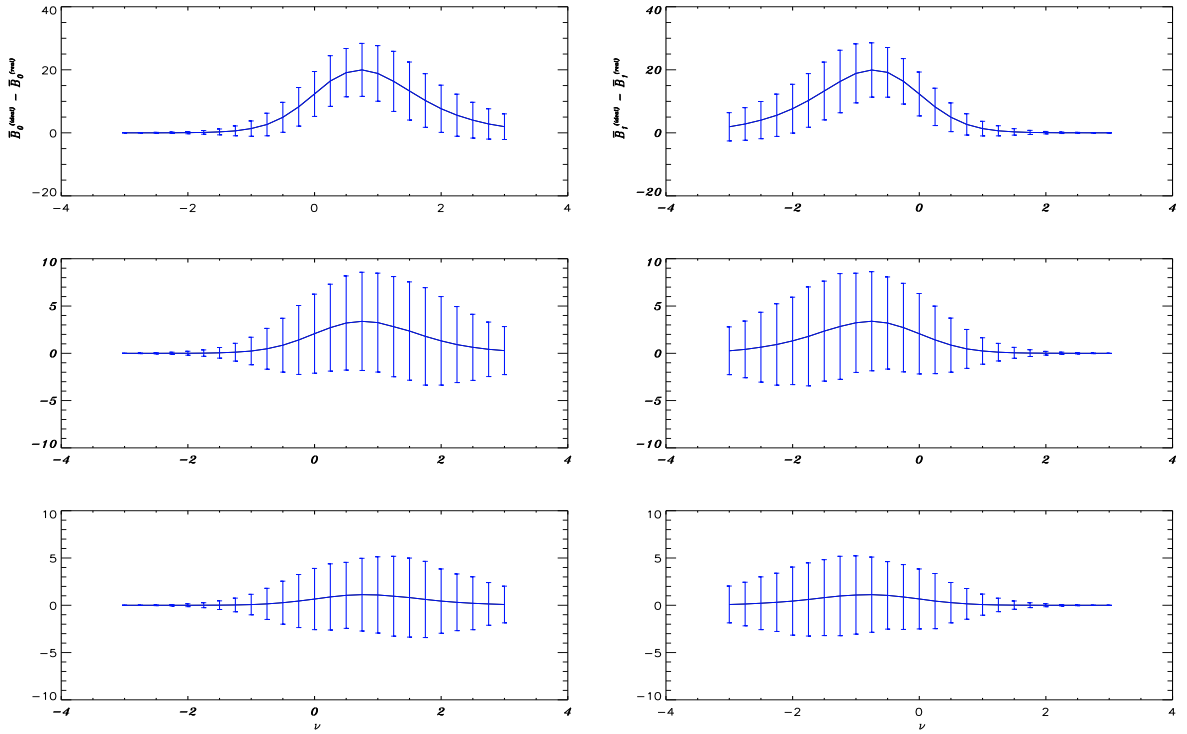


FIG. 7: The difference between the mean values of real and ideal case for the Betti numbers considering $r = 0$ over 500 simulations. From top to bottom: $\theta_s = 10', 40', 60'$, respectively. From left to right: the first and the second Betti numbers, respectively.

VI. CONCLUSIONS

The CMB primordial B -type polarization is the main target of future CMB observations since it provides the unique opportunity to directly probe the evolution of the universe in the inflationary stage. To avoid misunderstanding of the data, one must take into account the different sources of the observed B -mode signal, as for example, CMB weak lensing, astrophysical foregrounds and instrumental noises. It is well known that the unavoidable partial sky CMB analysis lead to a leakage from E to B mode, acting as an extra noise for the primordial signal. In this paper, we analyzed the effect of the E -to- B leakage in the measurement of the CMB B -mode. In order to clearly show the effect of leakage residuals, and exclude the effects of the other factors, throughout this paper, we do not consider the instrumental noises (depending on the specific experiment, and the survey

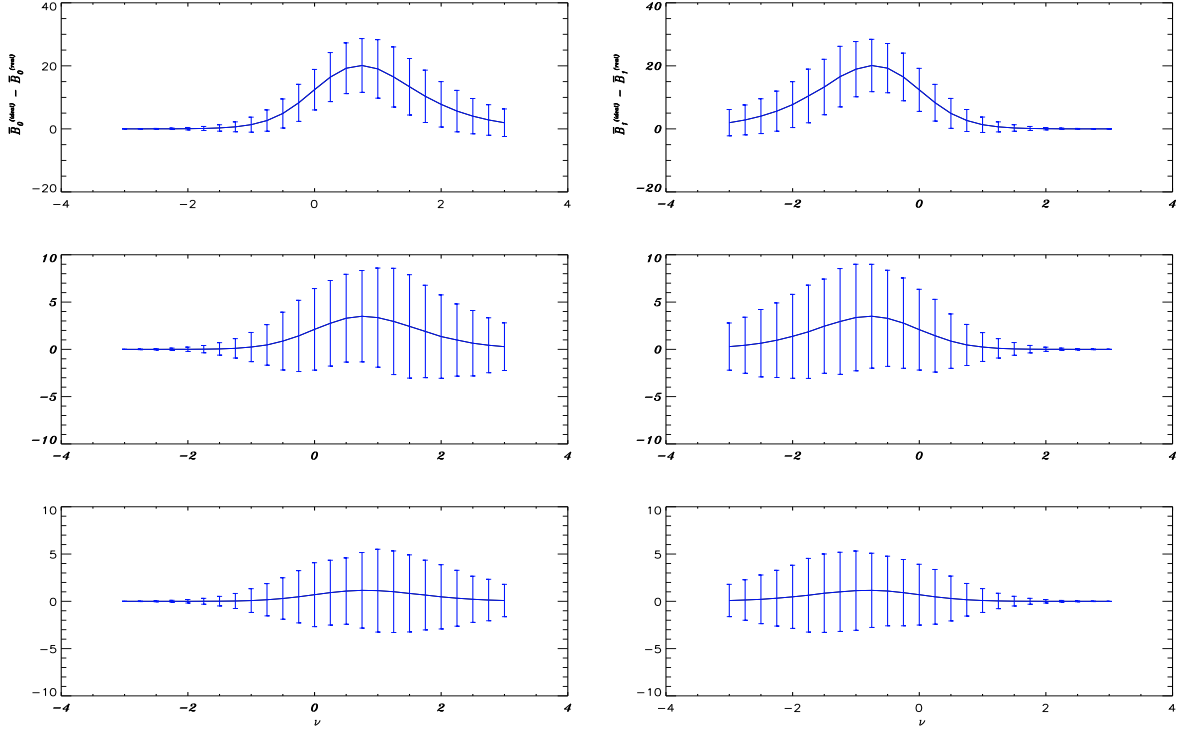


FIG. 8: The difference between the mean values of real and ideal case for the Betti numbers considering $r = 0.1$ over 500 simulations. From top to bottom: $\theta_s = 10', 40', 60'$, respectively. From left to right: the first and the second, respectively.

scheme) and the possible foreground radiations.

A number of practical methods have been developed for the E/B decomposition in the incomplete sky surveys. In this paper, we adopted the method suggested by Smith et al., which ensures the small error bars in all experimental configurations and leads to the smallest leakage residuals. In addition, this method is based on the algebraic framework of χ -field, which avoids the high computational cost and can be easily applied to the high resolution CMB maps. However, even if this separation method is used, the residual of the E -to- B leakage is left in the constructed \mathcal{B} -maps. In the present article, we employed the MFs, Betti numbers, skewness and kurtosis statistics to study the morphological imprint of the leakage in the \mathcal{B} -mode polarization maps. We compared the ideal case, in which the \mathcal{B} -maps were generated from full-sky Q and U observables, and the real case, where we generated the \mathcal{B} -maps after applying the smoothed Planck polarization mask UT78 to the Q and U sky by means of the Smith method described in [32]. Different from the real case, the ideal case is free from the E -to- B leakage residual caused by the E/B separations. So, the difference between these two cases reflects the imprint of E -to- B leakage.

First, we compare the power spectra of \mathcal{B} -mode polarization maps in these two cases, and found that they are nearly same, in particular in the low-multipole range, and the contribution of E -to- B leakage is tiny. Second, we did not find any imprint of the E -to- B leakage in the simulated \mathcal{B} -maps when considering both skewness and kurtosis statistics, which shows that these one-point statistics are not sensitive to the leakage. These results confirm the effectiveness of the E/B separation method.

However, by comparing the MFs and Betti numbers applied to the \mathcal{B} -mode maps generated in the ideal and real cases, we find that the effect of leakage residuals decreases quickly with the increasing of θ_s , which significantly shows that the residuals are dominant by the higher multipoles. This result is consistent with the one derived from the power spectrum analysis. In addition, we also found that the leakage cannot be ignored when combining the results of all the smoothing scales, θ_s , in both models, $r = 0$ and $r = 0.1$. Considering individual smoothing scales leads to the mistaken conclusion that the significance of the leakage is small and that it can be safely neglected. It is then important to point out that the large correlation of the MFs for different smoothing scales is expected since the leakage is not randomly distributed in the sky. The E -to- B leakage plays an important role in the final \mathcal{B} -map and must be taken into account to avoid misinterpretation of the data.

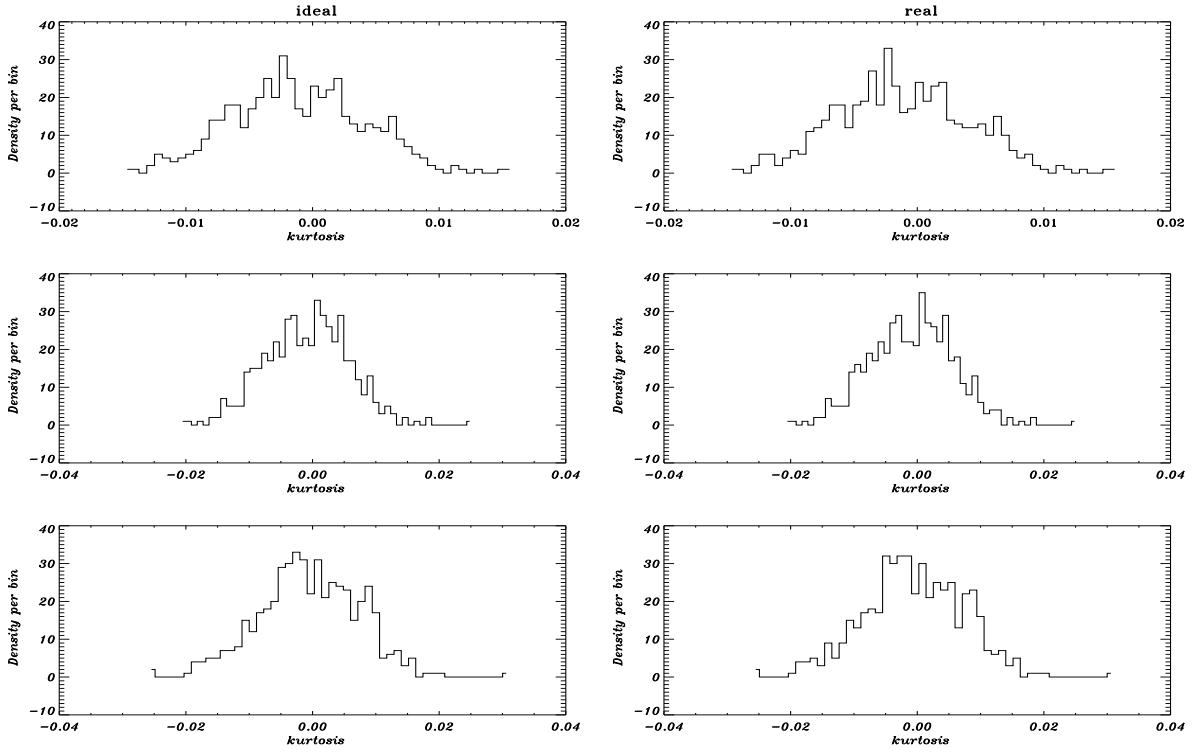


FIG. 9: The value for the skewness for 500 simulations considering $r = 0$ for the ideal and real cases as specified in the figure. From top to bottom: $\theta_s = 10', 40', 60'$, respectively.

Acknowledgements

We acknowledge the use of the Planck Legacy Archive (PLA). Our data analysis made the use of HEALPix [60], CAMB [59] and LensPix [57]. This work is supported by NSFC No. J1310021, 11603020, 11633001, 11173021, 11322324, 11653002, project of Knowledge Innovation Program of Chinese Academy of Science and the Fundamental Research Funds for the Central Universities.

-
- [1] D. N. Spergel, *et al.* (WMAP Collaboration), *Astrophys. J. Suppl.* **148**, 175 (2003); E. Komatsu *et al.* (WMAP Collaboration), *Astrophys. J. Suppl.* **192**, 18 (2011); G. F. Hinshaw *et al.* (WMAP Collaboration), *Astrophys. J. Suppl.* **208**, 19 (2013).
 - [2] P. A. R. Ade *et al.* (Planck Collaboration), *A&A* **571**, A1 (2014); P. A. R. Ade *et al.* (Planck Collaboration), *A&A* **571**, A16 (2014); N. Aghanim *et al.* (Planck Collaboration), *A&A* **594**, A11 (2016).
 - [3] U. Seljak and M. Zaldarriaga, *Phys. Rev. Lett.* **78**, 2054 (1997); M. Zaldarriaga and U. Seljak, *Phys. Rev. D* **55**, 1830 (1997).
 - [4] M. Kamionkowski, A. Kosowsky and A. Stebbins, *Phys. Rev. Lett.* **78**, 2054 (1997); *Phys. Rev. D* **55**, 7368 (1997).
 - [5] R. Adam *et al.* (Planck Collaboration), *A&A* **594**, A1 (2016); N. Aghanim *et al.* (Planck Collaboration), *A&A* **594**, A11 (2016).
 - [6] A. G. Polnarev, *Soviet Astronomy*, **29**, 607 (1985); J. R. Pritchard and M. Kamionkowski, *Annals Phys. (N.Y.)* **318**, 2 (2005); W. Zhao and Y. Zhang, *Phys. Rev. D* **74**, 083006 (2006); D. Baskaran, L. P. Grishchuk and A. G. Polnarev, *Phys. Rev. D* **74**, 083008 (2006); R. Flauger and S. Weinberg, *Phys. Rev. D* **75**, 123505 (2007).
 - [7] L. P. Grishchuk, *Sov. Phys. JETP* **40**, 409 (1975); *Ann. N. Y. Acad. Sci.* **302**, 439 (1977); *JETP Lett.* **23**, 293 (1976); A. A. Starobinsky, *JETP Lett.* **30**, 682 (1979); *Phys. Lett. B* **91**, 99S (1980); V. F. Mukhanov, H. A. Feldman, and R. H. Brandenberger, *Phys. Rept.* **215**, 203 (1992); D. H. Lyth and A. Riotto, *Phys. Rept.* **314**, 1 (1999).
 - [8] M. Zaldarriaga and U. Seljak, *Phys. Rev. D* **58**, 023003 (1998).
 - [9] W. Hu, *Phys. Rev. D* **65**, 023003 (2002).
 - [10] A. Lewis and A. Challinor, *Phys. Rept.* **429**, 1 (2006).
 - [11] D. Hanson *et al.* (SPT Collaboration), *Phys. Rev. Lett.* **111**, 141301 (2013); R. Keisler *et al.*, (SPTPol Collaboration), arXiv:1503.02315.
 - [12] P. A. R. Ade *et al.*, (POLARBEAR Collaboration), *Astrophys. J.* **794**, 171 (2014).
 - [13] S. Naess *et al.*, (ACTPol Collaboration), *JCAP* **10**, 7 (2014).
 - [14] P. A. R. Ade *et al.*, (BICEP2 Collaboration), *Phys. Rev. Lett.* **112**, 241101 (2014).

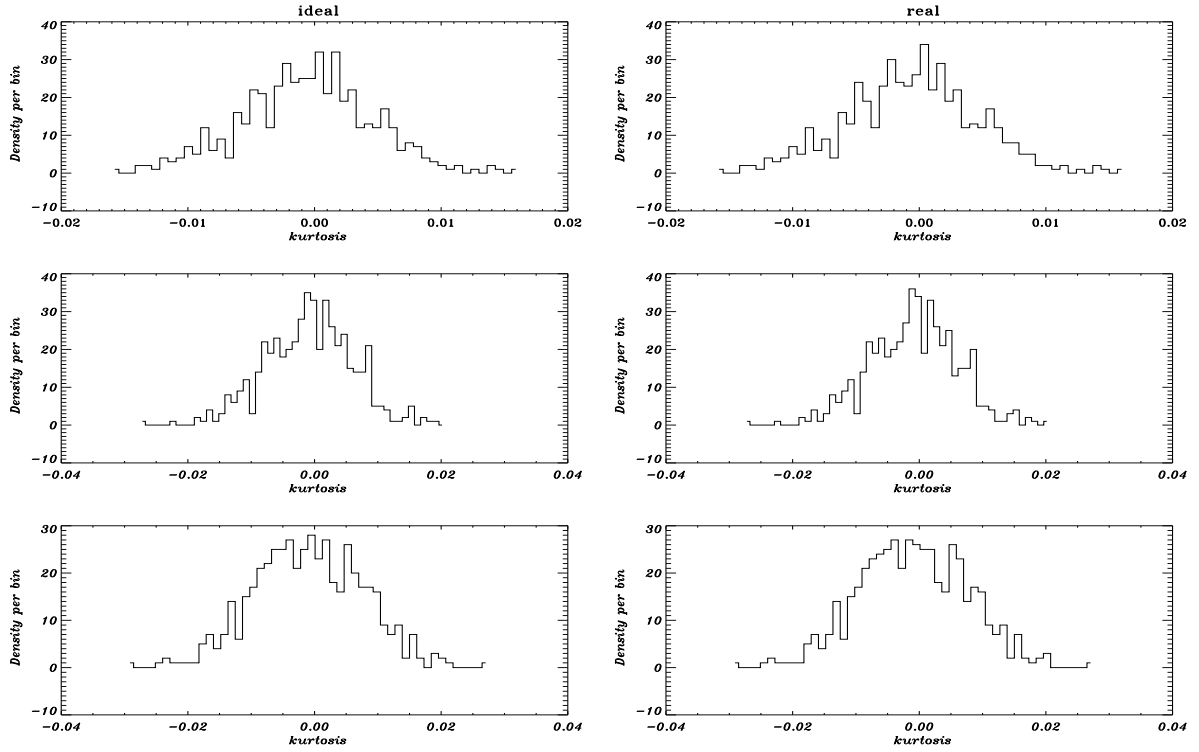


FIG. 10: The value for the skewness for 500 simulations considering $r = 0.1$ for the ideal and real cases as specified in the figure. From top to bottom: $\theta_s = 10', 40', 60'$, respectively.

- [15] P. A. R. Ade *et al.*, (BICEP2/Keck and Planck Collaborations), *Phys. Rev. Lett.* **114**, 101301 (2015).
- [16] P. A. R. Ade *et al.*, (BICEP2, Keck Array Collaborations), *Astrophys. J.* **811**, 126 (2015).
- [17] P. A. R. Ade *et al.*, (Keck Array and BICEP2 Collaborations), *Phys. Rev. Lett.* **116**, 031302 (2016)
- [18] P. A. R. Ade *et al.*, (Planck Collaboration), arXiv:1512.02882.
- [19] J. Bock *et al.*, *Task Force on Cosmic Microwave Background Research*, arXiv:astro-ph/0604101.
- [20] e.g. Q. G. Huang, S. Wang and W. Zhao, *JCAP* **10**, 035 (2015); P. Creminelli, D. L. Nacir, M. Simonovic, G. Trevisan and M. Zaldarriaga, *JCAP* **11**, 031 (2015); J. Errard, S. M. Feeney, H. V. Peiris and A. H. Jaffe, *JCAP* **3**, 052 (2016) ; and the references therein.
- [21] T. Matsumura *et al.*, (LiteBIRD Collaboration), *Journal of Low Temperature Physics*, **176**, 733 (2014).
- [22] D. Baumann *et al.*, (CMBPol Collaboration), *American Institute of Physics Conference Series*, **1141**, 10 (2009) arXiv:0811.3919; J. Bock *et al.*, arXiv:0906.1188.
- [23] C. Armitage-Caplan *et al.*, (CoRE Collaboration), arXiv:1102.2181.
- [24] P. Andre *et al.*, (PRISM Collaboration), arXiv:1306.2259
- [25] A. Kogut *et al.*, (PIXIE Collaboration), arXiv:1105.2044.
- [26] J. Bock *et al.*, *Task Force on Cosmic Microwave Background Research*, arXiv:astro-ph/0604101.
- [27] J. Dunkley *et al.*, (CMBPol Collaboration), *American Institute of Physics Conference Series*, **1141**, 222 (2009) arXiv: 0811.3915; B. Gold *et al.*, (WMAP Collaboration), *Astrophys. J. Suppl.* **192**, 15 (2011); P. A. R. Ade *et al.*, (Planck Collaboration), *A&A* **576**, A104 (2015); R. Adam *et al.*, (Planck Collaboration), *A&A* **594**, A10 (2016).
- [28] R. Adam *et al.*, (Planck Collaboration), *A&A* **586**, A133 (2016) .
- [29] A. Challinor and G. Chon, *MNRAS* **360**, 509 (2005).
- [30] E. F. Bunn, M. Zaldarriaga, M. Tegmark and A. de-Oliveira-Costa, *Phys. Rev. D* **67**, 023501 (2003); E. F. Bunn and B. Wandelt, arXiv:1610.03345.
- [31] A. Lewis, *Phys. Rev. D* **68**, 083509 (2003); L. Cao and L. Z. Fang, *Astrophys. J.* **706**, 1545 (2009); E. F. Bunn, *Phys. Rev. D* **83**, 083003 (2011); L. Thibaut, N. Sigurd, D. Sudeep, D. Joanna and S. Blake, *MNRAS* **435** 2040L (2013); J. Grain, M. Tristram and R. Stompor, *Phys. Rev. D* **79**, 123515 (2009).
- [32] K. M. Smith *Phys. Rev. D* **74**, 083002 (2006); K. M. Smith and M. Zaldarriaga, *Phys. Rev. D* **76**, 043001 (2007).
- [33] W. Zhao and D. Baskaran, *Phys. Rev. D* **82**, 023001 (2010).
- [34] J. Kim and P. Naselsky, *A&A*, **519**, A104 (2010);
- [35] B. Leistedt, J. D. McEwen, M. Büttner and H. V. Peiris, arXiv:1605.01414.
- [36] Y. F. Wang, K. Wang and W. Zhao, *Research in Astronomy and Astrophysics* **16**, 4 (2016).
- [37] A. Ferte, J. Grain, M. Tristram, R. Stompor, *Phys. Rev. D* **88**, 023524 (2013); A. Ferte, *Statistics of the CMB polarised anisotropies*, PhD Thesis (2015) [arXiv:1506.05940].

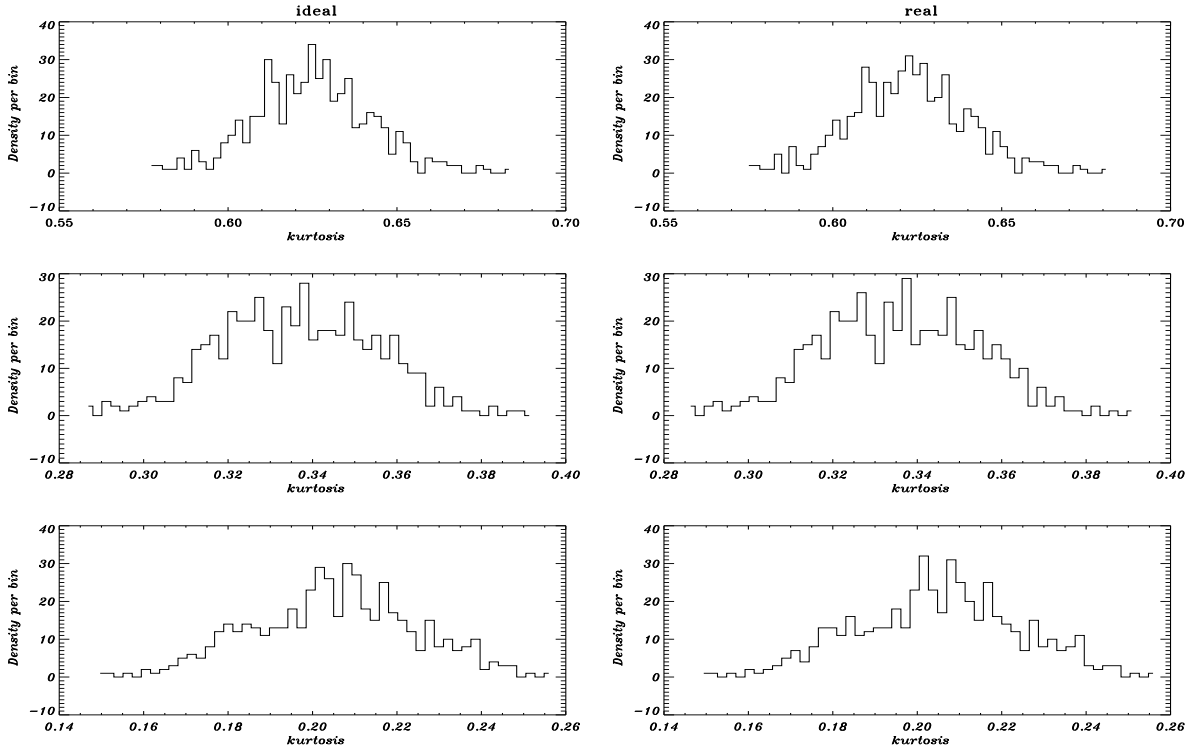


FIG. 11: The value for the kurtosis for 500 simulations considering $r = 0$ for the ideal and real cases as specified in the figure. From top to bottom: $\theta_s = 10', 40', 60'$, respectively.

- [38] L. Santos, K. Wang and W. Zhao, JCAP **07**, 029 (2016).
- [39] H. Minkowski, Mathematische Annalen **57**, 447 (1903).
- [40] J. R. Gott III, C. Park, R. Juszkiewicz, W. E. Bies, D. P. Bennett, F. R. Bouchet, and A. Stebbins, Astrophys. J. **352**, 1 (1990).
- [41] R. Schneider, *Covex bodies: the Brunn-Minkowski theory* (Cambridge University Press, Cambridge, 1993).
- [42] K. R. Mecke, T. Buchert and H. Wagner, A&A, **288**, 697 (1994).
- [43] J. Schmalzing and T. Buchert, Astrophys. J. **482**, L1 (1997).
- [44] J. Schmalzing and K. M. Gorski, MNRAS **297**, 355 (1998).
- [45] S. Winitzky and A. Kosowsky, New Astron. **3**, 75 (1998).
- [46] U. Seljak and M. Zaldarriaga, Astrophys. J. **469**, 437 (1996).
- [47] M. Zaldarriaga and U. Seljak, Phys. Rev. D **55**, 1830 (1997).
- [48] G. Efstathiou, MNRAS **349**, 603 (2004).
- [49] J. Kim, A&A, **531**, A32 (2011).
- [50] E. A. Lim and D. Simon, JCAP **1**, 408 (2012).
- [51] A. Ducout, F. R. Bouchet, S. Colombi, D. Pogosyan and S. Prunet, MNRAS **429**, 2104 (2013).
- [52] C. Gay, C. Pichon, D. Pogosyan, Phys. Rev. D, **85**, 023011 (2012).
- [53] P. Chingangbam, C. Park, K. P. Yogendran, R. van de Weygaert, Astrophys. J. , **755**, 122 (2012).
- [54] C. Hikage, E. Komatsu and T. Matsubara, Astrophys. J. **653**, 11 (2006).
- [55] V. Ganesan, P. Chingangbam, K. P. Yogendran and C. Park, JCAP, **2**, 028 (2015).
- [56] C. Hikage, T. Matsubara, P. Coles, M. Liguori, F. K. Hansen and S. Matarrese, MNRAS **389**, 1439 (2008).
- [57] <http://cosmologist.info/lenspix/>.
- [58] A. Lewis, Phys. Rev. D **71**, 083008 (2005); A. Lewis, A. Challinor and D. Hanson, JCAP **03**, 018 (2011).
- [59] <http://camb.info/>; A. Lewis, A. Challinor and A. Lasenby, Astrophys. J. **538**, 476 (2000).
- [60] K. M. Gorski, E. Hivon, A. J. Banday, B. D. Wandelt, F. K. Hansen, M. Reinecke and M. Bartelman, Astrophys. J. **622**, 759 (2005).

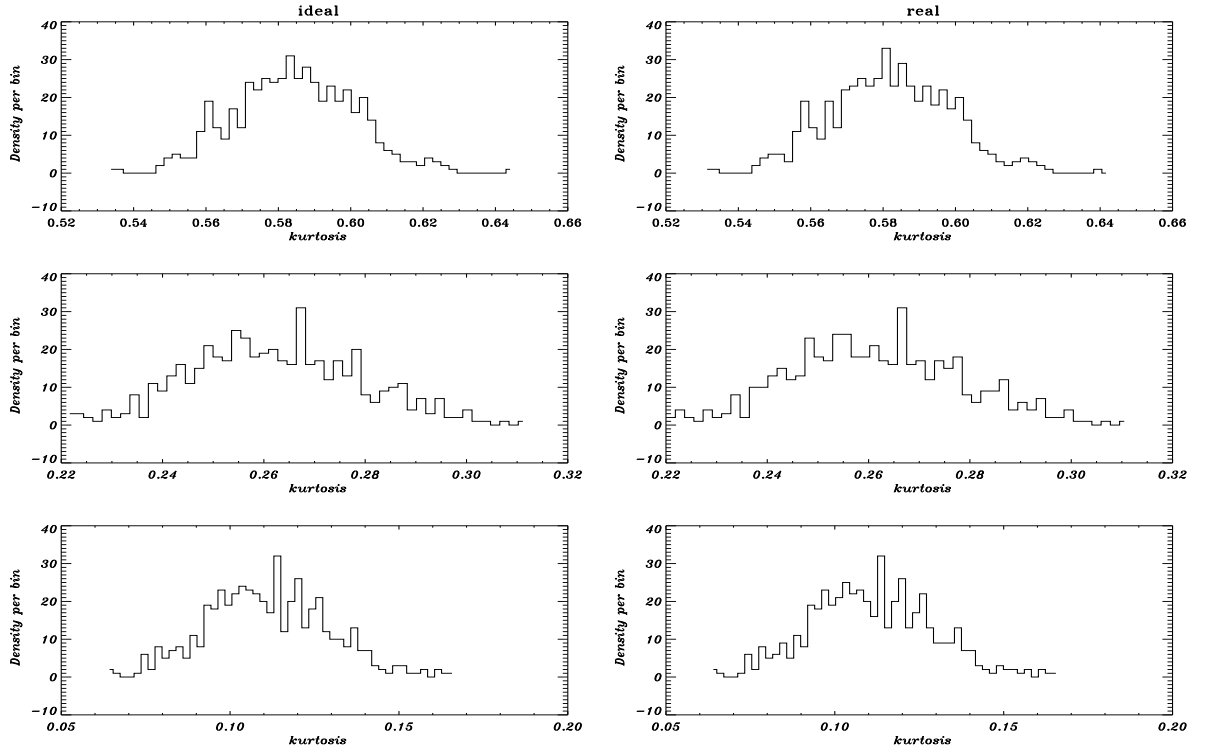


FIG. 12: The value for the kurtosis for 500 simulations considering $r = 0.1$ for the ideal and real cases as specified in the figure. From top to bottom: $\theta_s = 10', 40', 60'$, respectively.